CANCER IMAGING: Instrumentation and Application. Volume 2. Edited by M.A. Hayat. Page 3-16.

CHAPTER 1

Proton Computed Tomography

Jerome Zhengrong Liang, Tianfang Li, Reinhard W. Schulte, Todd J. Satogata,
David C. Williams, and Hartnut F.-W. Sadrozinski

1. INTRODUCTION

This chapter presents the principles of proton computed tomography (pCT) and reviews its clinical applications. The emphasis is on image reconstruction from projected data along proton paths which may not necessarily be straight lines through the object to be imaged.

The potential of pCT in medicine relies mainly on its role in improving proton beam therapy. Proton beams have distinct advantages compared to other radiation therapy options, such as X-rays, electron beams, etc, because they deliver radiation energy in a quite precise manner while leaving the normal tissues around a targeted tumor mostly unharmed or undamaged. This is possible due to the characteristics of the dose distribution along the proton path inside the body: a relatively low dose along the entrance toward the path end and a high dose peak at the end, called high-dose Bragg peak. Beyond the Bragg peak the dose falls off rapidly, i.e., from 90% to 20% of the peak dose within a few millimeters. Positioning the peak inside the target delivers a maximum dose to the tumor with minimal damage to the surrounding tissues.

By contrast, when an X-ray beam of therapeutic energy (at MeV level) traverses the whole body, it delivers radiation energy along its entire path in a relatively uniform manner (see the chapter by Meeks in this volume: Megavoltage Computed Tomography Imaging). If a tumor is

near a critical region like the spinal cord or the optic nerve, proton beams have a clear advantage by leaving the adjacent critical region unexposed regardless of the beam direction because of the Bragg peak, whereas X-ray beams can only avoid the critical structure if it is not on the beam path. Electron beams share a similar dose distribution as X-ray beams, except for a relatively shorter path. For example, by an X-ray beam of 6 MeV, a therapeutic dose can be delivered at a target ≥ 15 cm deep inside the body, while an electron beam of the same energy cannot effectively deliver a therapeutic dose beyond 5 cm (the effective path of electron beam is approximately half the energy quantity, i.e., 3 cm).

Due to the above advantages of proton beams, several medical proton accelerator facilities have been established during the past 15 years in the U.S. and Japan. Proton treatment facilities are now coming on line at major hospitals in the U.S. (e.g., Massachusetts General Hospital, Loma Linda University Medical Center, and University of Florida) and around the world. Over one hundred thousand patients have been benefited from these proton treatment centers.

In these existing proton treatment centers, the dose calculations are currently performed based on X-ray computed tomography (xCT, see the chapter by Bavenel in this volume: Multi-Detector Row Computed Tomography), and the patient is positioned with the help of X-ray radiographs, hence direct visualization of the three dimensional (3D) patient anatomy in the treatment room is presently impossible, limiting the accuracy of proton therapy. It is technically challenging to integrate xCT in the treatment room for patient position. In addition, the accuracy of xCT for proton treatment planning is limited due to the difference in physical interactions between photons and protons, which partially obviates the advantage of proton therapy. Using proton beam for the purposes of dose calculation and patient anatomy position in the treatment room would offer a great advantage in terms of convenience, cost effectiveness and achieving more

precise patient treatment. This is now recognized as the major motivation of developing pCT and also the major clinical application of proton beams for imaging.

2. REVIEW OF PRIOR STUDIES ON PROTON IMAGING

Several early publications have demonstrated the feasibility of proton beams for imaging. In the late 1960's, Koehler (1968) showed that with parallel-sided objects with a thickness nearly equal to the path length or range of an incident 160 MeV proton beam, proton radiographic films could be produced with much greater image contrast than that of X-ray radiographs taken under the same conditions. Since that time, a number of publications about proton radiography (Koehler and Steward 1974) and tomography (Cormack and Koehler 1976) have appeared in the literature, which mainly addressed proton imaging as a diagnostic tool (Hanson et al. 1981, 1982). However, because most of the technological development efforts successfully went into improving the diagnostic xCT in those decades, the interest in developing medical pCT stagnated.

The situation changed with the development of medical proton gantries for delivery of proton beams, first at Loma Linda University Medical Center, and now in several other proton treatment centers, resulting in an increasing number of patients treated with proton therapy. This new technical development and increase of patient number elevated the need for an accurate prediction of the proton dose distributions and verification of the patient position on the treatment table, and also demanded the development of accurate 3D imaging techniques. This has lead to a renewed interest in proton imaging and the construction of a proton radiography system at the Paul Scherrer Institute in Switzerland (Schneider et al. 2004).

Presently, a pCT system utilizing a proton gantry and fast image reconstruction techniques has not yet been developed. However, a recently published design study has concluded that a pCT

scanner should utilize instrumentation developed for high-energy physics such as silicon track detectors and crystal calorimeters equipped with fast readout electronics, allowing one-by-one registration of protons traversing the body during a full revolution of the proton gantry (Schulte et al. 2004). Different from proton beam therapy where the Bragg peak is positioned inside the targeted tumor inside the body, pCT may label each incident proton and detect that proton when it exits from the body by a high-energy detector where the high-dose Bragg peak will occur inside the detector. The pCT scanner will provide precise information on the proton's incident energy, location and direction, as well as its exit energy, location and direction. Another recently published study further concluded that a completely new image reconstruction paradigm is needed for pCT which deals with the proton path of curves, rather than the well-known X-ray path of straight lines in xCT (Li et al. 2006). An adequate image reconstruction algorithm shall utilize the pCT scanner measurements to map the energy loss along the proton trajectories through the body.

A successful implementation of pCT would avoid the ambiguities of mapping xCT Hounsfield units (HU, which is related to the X-ray attenuation coefficients) to electron densities, and would allow actual dose distribution and also verification of patient position in the treatment room. In other words, the availability of pCT in the treatment room will predict very accurately the position of the Bragg peak within the patient's body, resulting in a maximum dose delivery to the targeted tumor and successful sparing of the surrounding normal tissues. Furthermore, a successful integration of pCT with proton therapy may lead to the ultimate form of image-guided 3D conformal radiation therapy, which has the potential to deliver the optimal dose to any point within the patient and provide arbitrarily shaped inhomogeneous dose distributions as desired (see the chapter by Yap in volume two of this series: Cancer Therapy: Positron Emission

Tomography/Computed Tomography). This is now recognized as the major potential of pCT in medicine. The image formation principles of proton beam are presented below. Hardware configuration and data acquisition for pCT will be discussed. The emphasis will be on the issue of image reconstruction from projected data along proton trajectories through the body.

3. IMAGE FORMATION PRINCIPLES OF PROTON COMPUTED TOMOGRAPHY

Image formation for pCT, similar to other imaging modalities (e.g., see several chapters in this volume), relies on the interaction of incident energy with the tissues inside the body. The knowledge of the interaction and the accuracy of measuring the difference of the exit energy from the incident energy determine the quality of the reconstructed image about the body internals.

3.1 Interactions of Protons With Atomic Components of the Tissues Inside the Body

When traversing the body, protons lose some of their energy via inelastic collisions with the outer electrons of the tissue atomic components leading to ionizations and excitations. Furthermore, they will be deflected by multiple small-angle scattering (i.e., multiple Coulomb scattering -- MCS) from the nuclei of the tissue atomic components. These two main processes, occurring by a great number of times along the macroscopic path length of the protons, lead to the macroscopic effects of the interaction of protons with the tissues inside the body: (1) loss of energy and (2) deflection from their original direction. As individual interaction events occur randomly, these two processes result in a statistical distribution of the following two principal quantities observed for proton imaging: (1) the amount of energy lost by each proton after traversing the body, and (2) the lateral and angular displacements of the proton from its incident position and direction. The amount of energy-loss variation (i.e., energy straggling, which is reflected by the variation of the Bragg peak width of a proton traversing along the same path

through the same object) is the principal limitation for the intrinsic image contrast or density resolution of pCT (Satogata et al. 2003; Schulte et al. 2005). The variation of proton trajectory due to the random MCS, resulting in the lateral and angular displacements, is the principal limitation for the intrinsic image spatial resolution of pCT (Li et al. 2004, 2006). These two principal limitations will be discussed in more details later.

In addition to the above two main processes of inelastic collisions with the outer atomic electrons and deflection from the atomic nuclei due to MCS, protons in the energy range (at the MeV level) used for pCT also undergo nuclear interactions, leading to reduction of proton transmission in a depth-dependent manner. Protons undergoing nuclear interactions mostly deposit their energies locally and hence contribute to the dose within the patient without contributing to the image formation. This would be a concern in developing pCT for clinical use. Below we will briefly discuss the magnitude of this effect as a function of the thickness of the absorbing object before introducing the fundamental image formation equation of pCT. More quantitative discussion on proton absorption will be given later.

3.2 Energy Requirement and Tissue Characterization for Proton Computed Tomography

The protons used for pCT must have sufficient energy to penetrate the body to be imaged. According to the NIST PSTAR data base (National Institute for Standards and Technology, PSTAR database, http://www.physics.nist.gov/PhysRefData/Star/Text/PSTAR.html), the path depth or range in a continuous slowing-down approximation (CSDA) of 200 MeV protons in a tissue equivalent plastic is 25.8 cm, which is sufficient to penetrate an adult human skull (nominal width of 20 cm in anterior-posterior direction). For 250 MeV protons the range is 37.7 cm, sufficient to penetrate an adult trunk (nominal width of 34 cm, excluding arms). The relationship

between the average range and the incident energy for water may be approximately expressed as (Satogata et al. 2003):

$$< R >= 4.90k^2 + 2.77k \tag{1}$$

where R is in units of gram/cm^2, $k = E/100$[MeV], and E is the incident kinetic energy in units of MeV. Given an incident kinetic energy E in MeV, equation (1) predicts the average range of the proton in the water. At the energy levels greater than 200 MeV, protons are relativistic particles and their energy-velocity relationship is described by

$$\beta^2(E) = 1 - \left(\frac{E_p}{E + E_p} \right)^2, \quad \text{and} \quad \beta = \frac{v}{c} \tag{2}$$

where c is the light velocity (2.998×10^{10} cm/s), v the proton velocity, and E_p the rest mass of protons (938.3 MeV). For example, for 250 MeV protons, the relativistic velocity ratio is $\beta = 0.61$, which shall be considered in quantitative analysis of the proton energy loss.

The energy loss of protons after traversing the body is a measure of the integrated electron-density distribution along the proton path. More electrons are on the path, more interactions occur, and more energies loss. The electron density of a medium is defined as the number of electrons/cm^3. The relationship between the electron density ρ_e .and the physical density ρ is given by

$$\rho_e = \rho\, N_A \left(\frac{Z_e}{A_e} \right) \tag{3}$$

where N_A is Avogadro's number (6.022×10^{23}), and Z_e and A_e are the effective atomic number and atomic weight of the traversed object, respectively. Human tissues are composed of atoms of relatively low atomic number (Z) and weight (A) (ICRU Report No. 44, 1989). Since the ratio Z_e/A_e for the human tissues is fairly a constant, usually lies between 0.50 and 0.55, therefore the

electron density closely reflects the physical density of the tissues to be imaged. In other words, the intrinsic image contrast of pCT is somewhat directly related to the physical density contrast among the tissues. To avoid large numbers associated with absolute electron density values (at the order of 10^{23} electrons/cm^3), it is advantageous to express the results in terms of relative electron density, defined as:

$$\eta_e = \frac{\rho_e}{\rho_{e,water}} \tag{4}$$

where $\rho_{e,water} = 3.343\times10^{23}$ electrons/cm^3 is the electron density of water. For human soft tissues, the physical density ρ (or the relative electron density η_e) varies little between different tissues at the order of a few percent, and their density values scatter around that of water (ICRU Report No. 44, 1989). Thus pCT for the distribution of η_e inside the human body is inherently relative low contrast, similar to the xCT for the distribution of attenuation coefficients of soft tissues.

3.3 Mean Energy Loss and Integral Equation for pCT Image Formation

In the important energy range for pCT (10 – 250 MeV), the mean energy loss of protons per unit path length, also called stopping power *dE/dr*, is mainly due to the ionizations and atomic excitations and is well described by the Bethe Bloch theory. For protons in the stated energy range, corrections for density and shell effects are not required (Leo 1994). In this case, the Bethe Bloch formula may be written in the following form, convenient for pCT image reconstruction:

$$-\frac{dE}{dr}(r) = \eta_e(r)\, F[I(r), E(r)] \tag{5}$$

where η_e was defined before as the relative volume electron density to be reconstructed, and its dependence on the position vector $\boldsymbol{r}$ is a reminder that all quantities in equation (5) can vary with spatial position inside the body. The function $F[I(\boldsymbol{r}), E(\boldsymbol{r})]$ can be expressed as:

$$F(I(r),E(r)) = K\frac{1}{\beta^2(E)}\left[\ln\left(\frac{2m_ec^2}{I(r)}\frac{\beta^2(E)}{1-\beta^2(E)}\right)-\beta^2(E)\right] \quad (6)$$

where m_ec^2 is the electron rest energy (0.511 MeV), and $I(\mathbf{r})$ is the mean excitation potential of the material, which for water is about 75 eV (National Institute for Standards and Technology, Material Composition database, http://www.physics.nist.gov/cgi-bin/Star/compos.pl?ap). The constant K is defined as:

$$K = 4\pi\, r_e m_e c^2 \rho_{e,water} = 0.170\,\frac{\text{MeV}}{\text{cm}} \quad (7)$$

where r_e is the classical electron radius (2.818×10^{-13} cm).

Note that equation (5) is an approximation of the original Bethe-Bloch equation, which contains a term W_{max}, the maximum energy transfer in a single collision (Bichsel et al. 1972). This approximation is valid if the mass of the incident projectile is large relative to the electron mass, which is the case for protons. The Bethe-Bloch equation (5) is a non-linear first-order differential equation of the function $E(r)$. Since $I(r)$ is not known a priori, direct integration of this equation is intractable. However, for human tissues the variation of $I(r)$ is relatively small, and the dependence of the function $F(.)$ on $I(\mathbf{r})$ is relatively weak due to the logarithmic function in equation (6). Therefore, it is reasonable to assume that $I(r)$ is independent of location and can be replaced by the mean ionization potential of water I_{water} = 75 eV. In this case, $F(.)$ is only a function of E and equation (5) can be integrated as:

$$\int_{E_{out}}^{E_{in}} \frac{dE}{F(I_{water},E)} = p(I_{water}) = \int_S \eta_e(r)dr \quad (8)$$

where the integration on the left side can be calculated numerically, given the incident proton energy E_{in}, the exit proton energy E_{out} after traversing the body and the complicated energy

dependent function $F(.)$ of equation (6), as denoted by the notation $p(I_{water})$. The right side integration is along the proton path S. The relative electron density distribution $\eta_e(\boldsymbol{r})$ can be reconstructed based on the derived projection data $p(I_{water})$ (from measurements). Equation (8) resembles the format of the Radon transform for xCT if the proton path S is assumed as a straight line. Image reconstruction in pCT is to invert the path integral for the relative electron density distribution $\eta_e(\boldsymbol{r})$. Unlike the inversion in xCT, the proton path is unknown in pCT due to MCS and must be estimated. This uniqueness of pCT renders a challenge for image reconstruction from the projection data along an unknown path. In addition to this challenge and the approximation made for equation (5) from the original Bethe-Bloch equation, it shall be further noted that the integrated density along the proton path on the right side of equation (8) is approximated by the water-equivalent length of the proton trajectories through the body because of the use of I_{water} for calculation of the projection data $p(I_{water})$.

Equation (8) is the fundamental integral formula for image formation of pCT and is derived based on the energy interactions along the entire path through the body, ignoring the two main statistical processes of (1) energy loss straggling and (2) proton path uncertainty due to MCS, and the third one of proton absorption due to nuclear interaction. These three processes were briefly mentioned above and are now described in more details below.

3.4 Energy Loss Straggling

After traversing an object of certain thickness and density, monoenergetic protons will have experienced varying numbers of random collisions with the electrons along their paths. Further, the energy transferred by a proton to the atoms (mainly to their outer electrons) of the tissues is also subject to statistical fluctuations. In consequence, a monoenergetic beam incident on the

body will have an energy distribution after traversing the object, which was first described mathematically by Bohr (1948) and later by others.

For energy losses not exceeding 20% of the initial energy (> 20% loss will be discussed later), but large enough that the Central Limit Theorem applies, the energy-loss distribution is well described by a normal (Gaussian) distribution, for which only the first two moments of the distribution (i.e., mean and variance) are different from zero. For relativistic protons, the variance of the energy loss distribution after passing through a layer of thickness d can then be described by Bohr's theory as:

$$\sigma_B^2(d) = \eta_e K \int_0^d \frac{1-\frac{1}{2}\beta^2\left(E(E_{in},x)\right)}{1-\beta^2\left(E(E_{in},x)\right)}dx \qquad (9)$$

where $E(E_{in}, x)$ is the mean energy of protons of incident energy E_{in} after traversing a path length x inside the body, and η_e and K were defined above. For example, the spread of the energy loss after traversing the water of average range $< R >$ may be expressed by a root mean squares (RMS) measure as (Satogata et al. 2003):

$$\sigma_B(R) => \sigma_R[\text{MeV}] \approx 0.30 < R >^{1/2} \quad \text{or}$$

$$\sigma_R[\text{g/cm}^2] \approx 0.30(0.098k + 0.028) < R >^{1/2}) \qquad (10)$$

where σ_R is in units of MeV, $< R >$ is given by equation (1), and $k = E/100$[MeV] with E being the incident kinetic energy in units of MeV as defined before. For example, an incident 200 MeV energy would have an RMS energy spread of about 1.5 MeV or an RMS range spread of 0.34 cm by equation (10) at the end of its range of 25 cm in water. This intrinsic variation on the energy loss will ultimately affect the image contrast or density resolution of pCT as described below.

Successful implementation of pCT for applications in radiation therapy treatment planning requires that the relative electron density of the targeted tumor and surrounding normal tissues be determined with a high degree of accuracy (e.g., at the order of 1%), maintaining a sufficient degree of spatial resolution (e.g., at the order of 1 mm). The random noise in the energy measurement of outgoing protons will ultimately limit the ability to measure small density differences. Refer to xCT, where the principal noise limit is due to counting statistics of detected photons, pCT's principal noise limit is due to the energy straggling statistics of protons traversing the object. As in xCT, the only way to improve measurement accuracy is to increase the number of protons (if inaccuracy of detection system is not considered), thereby improving the statistics of the measurement. This will be at the cost of more radiation dosage. Therefore, it would be important to establish a dose-density discrimination relationship for a given density resolution (or image contrast) and voxel size, where the voxel size would reflect the proton beam flux as well as the spatial resolution (see the chapter by Martin et al. in volume two of this series: Radiation Dose and Image Quality). It is expected that the radiation dosage, image contrast and image resolution (voxel size) will be interrelated each other. The following gives a qualitative description.

The density resolution or intrinsic image contrast of a pCT scanner may be defined as the one-sigma spread of the derived relative electron density value with respect to its mean value, which in pCT is usually close to unity. It is assumed that this value is derived from the energy loss measurement of N protons traversing a given voxel of the object. Three main components contribute to the spread, (1) the energy loss straggling, (2) the energy or momentum spread of the incident protons, and (3) the noise of the energy measurement detector. Because we are mainly concerned with the principal density resolution limitation of pCT, we will assume that only energy loss straggling contributes to the pCT noise, and that the other two components can be

neglected. In other words, we only consider the primary cause due to energy loss straggling and ignore the other secondary effects.

Let $\Delta\eta_e$ be the incremental variation of the relative electron density in a cubic voxel of size *a*. The corresponding mean increment in outgoing proton energy for a proton traversing this voxel can be expressed as (Schulte et al. 2005):

$$\Delta E_{out} = \frac{dE}{dx} \cdot \Delta\eta_e \cdot a \tag{11}$$

where the stopping power *dE/dx* has to be evaluated at the location of the voxel. Assuming the relative electron density derivation is based on *N* protons traversing the voxel during the pCT scan, the energy loss straggling of individual protons, σ_B, will lead to a spread in the derived relative electron density given by

$$\sigma_{\eta_e} = \frac{\sigma_B}{\sqrt{N} \cdot a \cdot \left(\frac{dE}{dx}\right)} \tag{12}$$

where σ_B was defined before. Further, the dose delivered to the object at the location of the voxel may be expressed as:

$$D = \frac{N}{a^2 \cdot \rho_e} \cdot \left(\frac{dE}{dx}\right). \tag{13}$$

Solving equation (13) for *N* and substituting *N* into equation (12) gives the following useful relationship between relative electron density resolution and radiation dosage:

$$\sigma_{\eta_e} = \frac{\sigma_B}{\sqrt{D \cdot a^4 \cdot \rho_e \cdot \left(\frac{dE}{dx}\right)}}. \tag{14}$$

Equation (14) reflects the dose dependence of the density resolution for a given object diameter as well as the dependence of the resolution on object diameter and incident proton energy for a given

dose. For water medium, the number of needed protons N and the resulted dosage D can be estimated, for an object diameter equals to the energy range $< R >$ of equation (1), by (Satogata et al. 2003):

$$N\sigma_{\eta_e}^2 a^2 \approx 0.28k(4.9k + 2.8)(0.10k + 0.03)^2 \tag{15}$$

$$D\sigma_{\eta_e}^2 a^4 \approx 4.5\times10^{-11}k(4.9k + 2.8)(0.10k + 0.03)^2 . \tag{16}$$

For example, a single 200 MeV proton (k = 2) passing through a square pixel (or cubic voxel) of size 1 mm in water (of diameter 25 cm) delivers an average dose of about 7.2×10^{-8} Gy to the voxel. To achieve density resolution of σ_{η_e} = 1% in voxel size of a = 1 mm, N = 370,000 protons are needed to pass through each voxel in water, and the surface dose is D = 26 mGy (Satogata et al. 2003).

3.5 Multiple Coulomb Scatter and Proton Path Uncertainty

When passing through the object to be imaged, protons in the energy range used for pCT experience multiple small-angle deflections due to scattering at the nuclear potential of the target atoms leading to a macroscopic deviation from the original direction by up to a couple degrees and a displacement of the exit point with respect to the entry point by up to a few millimeters. More specifically, assume that the incident proton beam has zero size and zero angular spread (i.e., zero emittance), the transverse size of a 200 MeV beam acquires an RMS spread of transverse size of 0.65 cm at the end of its range of 25 cm in water (Satogata et al. 2003). This is the physical root cause of the poor reputation that proton radiography has historically acquired, due to the inevitable blurring in simple transmission images. Fortunately, while MCS is the main limitation of the spatial resolution of proton imaging as discussed elsewhere (Schneider and Pedfoni 1994; Williams 2004), it has a limited contribution to the energy loss spread of the

protons due to statistical variation in the path length of protons undergoing MCS in a layer of given thickness. Furthermore, with new detection technology development, the exit proton displacement and direction can be measured very accurately (Sadrozinski et al. 2003). This proton-to-proton tracking measurement on a 200 MeV incident proton's entrance and exit positions can reduce the RMS spread of transverse size from 0.65 cm to less than 0.1 cm at the end of its path range of 25 cm in water (Satogata et al. 2003). This retained 1 mm transverse size is mainly due to the proton path uncertainty inside the body, which is the intrinsic limitation of the spatial resolution of pCT (Williams, 2004; Li et al. 2003, 2004, 2006).

3.6 Proton Loss Due to Nuclear Interactions

When imaging with protons, one has to account for the chance that protons will undergo nuclear interactions that may lead to an abrupt energy loss and/or large deflections. The probability of inelastic nuclear interactions of protons in the energy range used for pCT becomes significant above 100 MeV. Nuclear interactions result in a reduction of proton transmission with increasing thickness of the traversed object and thus contribute to unwanted patient dose. Janni (1982) tabulated the probability that a proton of a given initial energy will undergo at least one nuclear interaction during its path length. For 250 MeV protons, which have a CSDA range of about 38 cm, this probability was given as 30%. The ICRU Report 49 (1993) lists probabilities of at least one nuclear interaction for protons with initial energies from 100 to 1,000 MeV for different path lengths ranging from 1 cm to 100 cm. For example, the probability of a 200 MeV proton to be transmitted without undergoing a nuclear interaction is 92.2% for a water layer of 10 cm thickness, and 83.6% for a layer of 20 cm thickness. Although the probability of occurring at least one nuclear interaction for proton of 200 MeV to traverse a water layer of more than 20 cm thickness can be as high as 20%, the likelihood of the proton being absorbed inside the layer

remains to be determined. If the proton is deflected and then escapes the absorption inside the body, its majority energy may not contribute to the dose to the body.

4. DETECTOR DESIGN AND DATA ACQUISITION FOR PROTON CT

As discussed above, pCT system shall use the proton-to-proton tracking measurements to reduce the beam transverse spread due to the MCS. In the same time, the detector shall have an excellent energy resolution to measure accurately the energy loss after the proton exits from the body. A prototype system design for the proton-to-proton tracking measurements and high energy resolution is described below.

4.1 Design of a Proton Computed Tomography Scanner

Figure 1 illustrates our conceptual design of an idea pCT system which has the potential to label each incident proton and also measure its exit energy, location and direction (Sadrozinski et al. 2003; Schulte et al. 2004). The object is traversed by a broad (ideally but not necessarily parallel) beam of protons of known energy E_{in}. Using an active proton beam scanning system, the incident energy E_{in} may be adjusted, while scanning around the object, to optimize the density resolution according to spatial variations of the object thickness. A detector system is arranged on both sides of the object and records the exit energy E_{out} of individual protons, as well as their entrance and exit locations and directions with respect to the detector system. An experimental realization of the design is reported below.

4.2 Acquisition of Proton Radiography by the Proton Computed Tomography Design

Our initial experiment setup of Figure 1 was installed on the research beam line of the medical proton synchrotron at Loma Linda University Medical Center. A monochromatic 250 MeV

proton beam was degraded by a 25.4 cm thick (approximately cube-shaped) wax block ($\rho = 0{:}926$ gram/cm^2) to a mean energy of about 130 MeV. At a distance of 25 cm downstream from the wax block, the beam encountered the image object, a 5.0 cm long hollow aluminum cylinder $\rho = 2.7$ gram/cm^2) of outer diameter of 3.0 cm and inner diameter of 0.68 cm. Behind the object, protons were individually detected by two silicon detector modules, each consisting of a pair of single-sided silicon strip detectors (SSDs) with strips oriented at right angle to each other (see the four detector planes in Figure 1). These detectors, located immediately behind 27 cm downstream of the object, served to measure the spatial coordinates (*x* and *y*), the exit angles, and the energy of the protons that passed or traversed the object.

The data collected in our experiment was comprised of *x*- and *y*-hit positions and time-over-threshold (TOT) values from the four silicon planes. Proton transmission images were calculated for each SSD module by averaging the proton energy over a large number ($\approx 10^6$) of individual events, and displayed as 2D maps of proton energy versus the *x*- and *y*-strip positions in the respective SSD module. It was found that the image measured with the downstream module (SSD planes 3 and 4) showed almost no object features. This can be explained by the effect of multiple scattering. The 2D plot in Figure 2 (left) shows the spatial distribution of average energy in the upstream module for proton energies averaged in four by four strip pixels ($\approx 0.8\times0.8$ mm^2) or the proton energy averaged over pixels of 4×4 strips (pixel size $\approx 0.8\times0.8$ mm^2). The image of the phantom projection is clearly seen in the spatial energy distribution. Note that the coloring of the structure in Figure 2 (left) is directly proportional to the energy loss in the aluminum object and thus is proportional to the product of its length and density. Figure 2 (left) thus demonstrates the principle of image formation based on the proton-to-proton tracking spatial measurements of

proton energy loss behind the image object. Future work will be devoted to improve the accuracy of the energy loss and proton-to-proton tracking measurements.

To better understand the features of the proton transmission images, we performed simulations using the GEANT4 Monte Carlo (MC) toolkit (Agostinelli et al. 2003). Figure 2 (right) shows the measured and simulated angular distributions of protons in two areas or regions of interest (ROIs) in the transmission image: area A contains only protons, which traverse the object in its entirety, while area B contains protons which miss the object completely. The difference between the distributions was caused by the increased MCS inside the object. The agreement between data (symbols) and simulations (histograms) is good in both areas. Because of this good agreement of MC simulation with the experimental data, in the following studies the GEANT4 MC toolkit was used to simulate pCT projection data and investigate image reconstruction algorithm performance on the data.

5. IMAGE RECONSTRUCTION ALGORITHMS

Equation (8) is the mathematical expression of image reconstruction problem in pCT, where the projected data $p(.)$ are derived from the measurements of the energy loss of each incident proton and of the lateral and angular displacements from its incident direction. Four different categories of image reconstruction algorithms are reviewed below.

5.1 Filtered Backprojection Reconstruction Algorithm

Filtered backprojection (FBP) reconstruction algorithm was established mathematically for the inversion of the Radon transform, widely used in xCT. A fundamental assumption in the Radon transform is that the integral path S in equation (8) is a straight line. This assumption could be satisfied by approximating the actual proton path inside the body as a line connecting the entry and exit positions (see the line AB in Figure 3). This line is called straight line path (SLP).

Here we limit our illustration in two dimensions. The third dimension normal to the *t*-*u* plane is not considered. At the scanning angle of zero degree (i.e., horizontal direction from left to right in Figure 3), each proton may have a different path inside the body, resulting in a corresponding path line which may not be parallel to the line AB. Since we limit our illustration in the *t*-*u* plane, those lines which are not in the plane will not be considered. After rotating the incident proton beams over 180 degrees counterclockwise, we would collect various path lines which should span at least over 180 degrees in the *t*-*u* plane and therefore satisfy the sampling requirement for inversion of the Radon transform. The inversion of these measurements along their SLPs gives the 2D distribution image of $\eta_e(t,u)$.

By interpolating these straight lines into *M* groups such that in each group the lines are parallel to each other and equally spaced on *t* axis, then the image reconstruction becomes an inversion of the Radon transform from *M* projections (Li et al. 2003). The inversion has been solved exactly and efficiently by FBP algorithm. Given the fundamental image formation equation (8) for pCT, the FBP reconstruction is accurate up to the limit where the actual proton path can be approximated by straight lines. In reality, the approximation is not acceptable because the line could be off from the actual path curve by a few millimeters (see Figure 3). If the actual path is not a straight line, inversion of equation (8) by a FBP-type algorithm remains so far an open problem to be solved. In the following, we explore alternative algorithms if the actual path curve can be estimated.

5.2 Estimation of Proton Path

Using a Gaussian approximation of MCS and a χ^2-formalism, it was recently shown that it is possible to construct a closed-form expression for the most likely path (MLP) of a proton in a uniform material incorporating the effect of continuous energy loss when the entrance and exit

positions and angles are measured by the pCT system of Figure 1 with good accuracy (Williams 2004). This proton path estimate technique also provides estimates of the probability of the particle to deviate from the MLP and could be utilized in image reconstruction (to be discussed later). Further, it was shown that the MLP predicts the true path to better than 1 mm despite of the broadening of a needle beam to a size of several millimeters under typical pCT conditions. This prediction suggested the choice of 1 mm^3 voxel size in our numerical calculations above. An example of MLP is shown in Figure 4. Another proton path estimate technique fits the most smooth curve by cubic spline as the proton path (called cubic spline path -- CSP) using the measured entry and exit positions and directions (Li et al. 2006). This CSP does not assume the object is made from a uniform material, but also does not consider the physics of MCS, and therefore its accuracy could be potentially compromised. Given the estimated proton path, iterative algorithms are a choice to reconstruct the electron density distribution image $\eta_e(t,u)$. This is because iterative reconstruction algorithms trace the energy loss along the path for an estimate of the projection data and then utilize the difference of the estimated and actual measured projection data to refine the reconstruction iteratively until the difference becomes very small as defined by some criteria (Li et al. 2004)

5.3 Algebraic Reconstruction Algorithm

Algebraic reconstruction technique (ART) is a typical example of iterative reconstruction algorithms and was specifically tailored for xCT tomographic image reconstruction. It can be mathematically expressed as:

$$\eta_e^{(n+1)} = \eta_e^{(n)} + \frac{\mathbf{H}^T[\,p - \mathbf{H}[\eta_e^{(n)}]]}{\mathbf{H}^T[\mathbf{H}[\mathbf{1}]]} \tag{17}$$

where **H**[.] is the operator for forward projection and symbol *T* denotes the transpose operation, i.e., $\mathbf{H}^T[.]$ is the operator for backward projection. The denominator is the normalization constant relating to the projection operations. Index *n* is the iteration number. The notation η_e denotes, as defined before, the relative electron density vector to be reconstructed and *p* the projection data of the relative electron density derived from the measured energy loss using the right integral of equation (8). The forward and backward projections are usually performed by weighted summation using the intersecting lengths of each path with the associated voxels on that path in the object. In other words, the value of H_{ij} is the intersecting length of path *i* with image voxel *j*. The forward projection operator $\mathbf{H}[\eta_e^{(n)}]$ traces along path *i* through the *n*-th iterated reconstruction $\eta_e^{(n)}$ in the image domain for an estimate of the projection data p_i. The difference $p_i - \mathbf{H}[\eta_e^{(n)}]_i$ is then backprojected by operator $\mathbf{H}^T[.]$ along path *i* and scaled by the corresponding denominator (or the normalization constant) before being added to the first term $\eta_e^{(n)}$ on the right of equation (17) to obtain the (*n*+1)th iterated estimate of all voxels on that path *i*, i.e., those voxel values $\eta_e^{(n+1)}$ on path *i*. The forward and backward operators along each path *i* and the weighted update for next iteration estimation along that path make a beautiful piece of art architecture for this ART algorithm for tomographic imaging. The iterative reconstruction process is terminated when the difference of successively iterated estimates satisfies a criterion (say less than 0.1%) or a pre-set maximum iteration number is reached.

A MC simulation study is reported below which shows the difference between FBP and iterative ART algorithms as well as the difference of using different proton paths of MLP and CSP for the same iterative ART reconstruction algorithm. The phantom used for the pCT scan simulation is shown in Figure 5. For characterization of the spatial resolution, it contains two sets

of line patterns (strips) arranged on a circle and embedded within a water phantom with elliptical cross section simulating the human head with a longitudinal diameter of 16 cm, a transverse diameter of 14 cm, and a height of 20 cm. The first set of strips has ICRU-compact bone density (ICUR Report No. 49, 1993), while the second set comprises strips with air density. The line-pair density each set of strip patterns are 2.0, 2.5, 3.0, 3.5, 4.0, 4.5, 5.0, and 6.0 line pairs per cm (lp cm^{-1}). The elliptical water phantom is surrounded by a 1 cm thick shell of ICRU compact bone density, simulating the human skull.

Proton beams of 200 MeV were generated using the GEANT4 (version 6.2) for the pCT scanner of Figure 1 with 50,000 protons randomly distributed along the *t*-axis over a length of 24 cm at each projection angle. The incident beams were idealized parallel beams on the *t*-axis. The beams inside the object were idealized fan-type beams confined to the *t*-*u* plane for a 2D simulation for simplicity (see Figure 3). (If a proton is scattered out from the *t*-*u* plane by MCS, it is ignored. If these scattered protons are considered, a fully 3D reconstruction would be pursued. This is a future research topic.) A total of 180 projections were acquired, evenly distributed over 360^{o}. The dose to the center of the phantom was estimated using the formalism to determine the proton dose to a circular water phantom described previously (Schulte et al. 2004). To adapt this formalism to the present phantom, the bone shell was converted to a shell of 1.9 cm water-equivalent thickness (WET), and the resulting uniform ellipse (ignoring inserts) was converted to a circular disk of identical area with a WET of 8.8 cm and a height of 1 mm. The dose at the center of the disk resulting from the 180 projections with 50,000 protons per projection was calculated to be 3.5 mGy. The relevant entry and exit data of each proton including the position in the (*t*, *u*) entry plane (*u* = 0 cm), exit energy and position in the (*t*, *u*) exit plane (*u* = 30 cm), and exit direction projected onto the (*t*, *u*) plane (see Figure 3), were stored in the computer. The

position and direction data were used to calculate the path estimates for each proton within a "virtual" circular object boundary of 22 cm diameter. One should note that due to MCS, the exiting protons were no longer confined to the *t*-*u* plane. In order to limit the reconstruction to a 2D case, the coordinate in the direction vertical to the *t*-*u* plane was set to zero, i.e., confining the exit protons in the *t*-*u* plane and ignoring those protons which were scattered out the *t*-*u* plane. The energy information for each proton was used to compute the energy lost in the object as well as the integrated relative electron density along each proton path by the use of equation (8).

By the use of the FBP algorithm, the simulated pCT data of the elliptical phantom were first interpolated so that all the approximated SLPs were sampled into 180 parallel-beam projections evenly spaced over 360^{o}. These interpolated data were then reconstructed by the FBP algorithm with the Ramp filter at the Nyquist cutoff frequency. The reconstructed image is shown on the top left of Figure 5. By the use of the iterative ART algorithm, three kinds of estimated proton paths were considered for the forward- and backward-projection operators. The first kind was the approximated SLPs of the 180 projections over 360^{o} without the interpolation. The ART reconstruction is shown on the top right of Figure 5. The second kind was the estimated CSPs and the reconstructed image is shown in the middle left of Figure 5. The third kind was the estimated MLPs assuming a uniform medium of water and the reconstructed image is shown on the middle right of Figure 5. A pixel size of 0.25 mm was used for all the reconstructions. The initial image for ART algorithm was set to be zero, and satisfactory reconstructions were obtained after 120 iterations in all cases. It is seen that the SLP-based reconstruction (by either FBP or ART algorithms) shows a considerable loss of spatial resolution, with a resolution of about 2.5 lp cm^{-1} for the air-density pattern and about 2 lp cm^{-1} for the bone-density pattern. The FBP reconstruction seems better than that of ART with SLPs. This difference is due to different

algorithm performances. Due to the mismatch of assumed SLPs to the true proton paths, the ART may need much more iterations to achieve a good reconstruction, while FBP does not have this convergence problem. In comparison, tracing the proton paths with CSP or MLP for the ART reconstruction demonstrates observable improvement (than the SLP-based reconstructions) in spatial resolution to about 5.0 and 4.5 lp cm^{-1} for the air-density pattern and the bone-density patterns, respectively. The ART reconstruction with either the CSP estimate or the MLP estimate seems to generate similar image quality. This is understandable because the phantom is made mostly by water and the true proton path is expected to be smooth except for small changes around the air and bone strips. However, some small difference can be seen from their zoomed strips on the bottom of Figure 5.

The ART algorithm seeks iteratively a solution which matches the estimated projection data (by the forward projection operator) with the measured data until a pre-set criterion is satisfied or a pre-set maximum iteration number is reached. It does not consider the data statistics. Statistical model-based image reconstruction algorithms model the data statistics and incorporate any other available constraint for a statistically optimal solution (Liang et al. 1989). This kind of statistics-based image reconstruction algorithms has not yet explored for the pCT data of Figure 1. An example of statistics-based image reconstruction algorithms is given below.

5.4 Penalized Maximum Likelihood Reconstruction Algorithm

Given the approximated Gaussian distribution of energy loss due to the inelastic collision with atomic electrons (see sections 3.1 and 3.4 above), a penalized weighted least-squares (PWLS) approach would be a choice as a statistical model-based image reconstruction algorithm. The PWLS approach aims to minimize the cost function of

$$\Phi(\eta) = (p - H\eta)^T \Sigma^{-1} (p - H\eta) + \alpha\, Q(\eta) \tag{18}$$

where η represents η_e and Σ is a diagonal matrix with the diagonal value being the corresponding variance of a datum. The first term in equation (18) is the WLS measure of $\Phi(\eta) = (p - H\eta)^T \Sigma^{-1} (p - H\eta)$ which models the data statistics. The second term is a penalty which incorporates any other available constraint, where α is a smoothing parameter which controls the degree of agreement between the estimated and the measured data. The penalty is usually chosen as a quadratic form of

$$Q(\eta) = \eta^T Q \eta = \tfrac{1}{2} \sum_j \sum_{m \in N_j} w_{jm} (\eta_j - \eta_m)^2 \tag{19}$$

where index j runs over all image elements in the image domain, N_j represents the set of eight neighbors of the j-th image pixel in two dimensions. In the 2D case, the parameter w_{jm} is equal to 1 for the vertical and horizontal first-order neighbors and $1/\sqrt{2}$ for the diagonal (second-order) neighbors. The task for PWLS image reconstruction is to estimate the electron density distribution map $\eta(.)$ from the derived measurements or projection data $p(.)$:

$$\eta = \arg\min_{\eta \geq 0} \Phi(\eta)\,. \tag{20}$$

There are many numerical methods which can be employed to calculate iteratively the solution of equation (20). One would be the conjugate gradient method (Luenberger 1984). A simple numerical method could be the Gauss-Seidel (GS) update strategy (Sauer and Bouman 1993) or the well-known iterated conditional modes (ICM) strategy. A sophisticated iterative expectation-maximization (EM) update strategy could be another choice for the data of Gaussian distribution (Dempster et al. 1977; Liang and Ye 1994).

In the above statistical model-based image reconstruction, the proton path is estimated prior to the reconstruction. This implementation could be modified by adding an update of the proton path estimation into each iterative cycle of image reconstruction. In other words, after the *n*-th iteration, we would have obtained both $\eta^{(n)}$ and $S^{(n)}$, where the initial $\eta^{(0)}$ is chosen as uniform and $S^{(0)}$ is given by the CSP or MLP estimate. From the current ($\eta^{(n)}$,$S^{(n)}$), the update for $S^{(n+1)}$ can be performed by for example MC simulation. From the updated $S^{(n+1)}$ and current $\eta^{(n)}$, the forward and backward projection operators can be applied to obtain the update $\eta^{(n+1)}$. This interleaved approach had been explored for simultaneous image reconstruction and regions-of-interest (ROI) segmentation (Liang et al. 1991). In addition to the above four different categories of image reconstruction algorithms of (1) FBP with interpolated SLPs, (2) iterative ART, (3) statistics-based minimization and (4) interleaved update of proton path and electron density distribution map, there may be other alternatives. One can be a joint minimization for both proton path and electron density distribution map.

6. DISCUSSION AND CONCLUSIONS

Proton radiation therapy is one of the most precise forms of non-invasive image-guided cancer therapy. At present, the potentials of proton therapy cannot be fully exploited because the conversion of HU values, measured with xCT, to relative electron density values is not always accurate (Schaffner and Pedroni 1998). The resulting range uncertainty is usually quoted to be between 3 and 10 mm or 3% of the proton range in tissue, depending on the anatomical region treated and the penetration depth of the proton beam (Schneider and Pedroni 1998). In the studies (Satogata et al. 2003; Schulte et al. 2005), we have explored the principal limitations of pCT image contrast (or density resolution) and spatial resolution due to energy loss straggling and

MCS in the body. Some results were reviewed in section 3 above. By the use of pCT system design of Figure 1, one may be able to reduce the range error in proton treatment planning and delivery to less than 3 mm without exceeding practical dose limits. Our results confirmed this expectation that with a dose of about 10 mGy, which is clinically acceptable, the desired density resolution of 1% in the center of a cylindrical object of 20 cm and the desired spatial resolution of 1 mm can, in principle, be achieved. This indicates the potential of pCT to improve current xCT-based treatment planning for proton therapy.

The use of cone beam xCT scanners utilizing the rotating gantry of a linear accelerator in the treatment room has become a major innovation for alignment verification and image-guided x-ray photon radiation therapy in recent years (Jaffray et al. 2002; Seppi et al. 2003). Patient exposure is an important consideration in this new technology (Groh et al. 2002). Both therapeutic megavoltage (MeV) radiation and kilovoltage (keV) x-ray tubes mounted on the accelerator gantry in combination with flat-panel imaging systems have been tested. Doses required to distinguish soft-tissue structures in cylindrical phantoms are of the order of 1 cGy (10 mGy) for keV systems but are of one order of magnitude higher for MeV systems (due to the low detection efficiency of photon detectors in the MeV energy range) (Groh et al. 2002). According to our results, the doses required for soft-tissue density resolution with pCT will be similar to those for keV xCT. Proton CT, however, would have the advantage of using the same radiation modality for both treatment and imaging.

So far we have considered multiple Coulomb scatter (MCS) and energy loss straggling as the only uncertainty components contributing to the density and spatial resolutions, thus neglecting external noise sources such as the momentum spread of the proton accelerator and the uncertainty of the energy detector. Some additional spread may be introduced by beam line detectors such as

fluence and beam centering monitors. These effects seem small, but need to be investigated. Our dose estimate above did not take into account the loss of protons by nuclear interactions. In order to make up for these losses, one would need to increase the dose by corresponding amounts. The additional dose needed may be up to ~30% from what was estimated above if objects of 30 g cm^{-2} (equivalent to 30 cm of water) have to be penetrated and less for smaller objects. Thus the dose needed to reach 1% density resolution would increase from 10 mGy to 13% more for thick objects.

In equation (8), which is central to the reconstruction of pCT images, we have replaced the mean excitation potential $I(\boldsymbol{r})$ of the material traversed with that of water as a tissue substitute. This simplification may lead to systematic errors in the estimation of the line integral of the relative electronic density when the object contains materials with mean excitation potentials very different from that of water. Mean excitation potentials of various tissues have been published by the ICRU (1989) and are available from the NIST material data base (National Institute for Standards and Technology, Material Composition database, http://www.physics.nist.gov/cgi-bin/Star/compos.pl?ap). For example, for adipose tissue, muscle tissue, and compact bone the mean excitation potentials are 63.2 eV, 74.7 eV, and 91.9 eV, respectively, while the value for water is 75 eV. Corresponding errors in the stopping power (dE/dx) resulting from using the water value instead of the true tissue specific value can be calculated to be -2% for adipose tissue and +2% for compact bone, while for muscle tissue the error is practically zero (ICRU, 1993). This means that if the tissue evaluated with pCT consisted entirely of fat or bone, an additional density error of ± 2% would be introduced. However, as most body sections contain a mixture of these tissues, the actual systematic error due to the use of the mean excitation potential for water will be smaller than 2%.

In inverting the path integral of equation (8) for pCT, we have concluded that the approximation of straight line path (SLP) is not acceptable and the proton path must be estimated. Two estimated proton paths of most likely path (MLP) and cubic spline path (CSP) have been implemented with similar improvement over the SLP. By carefully inspecting the ART reconstructed images from MLP and CSP, the result from MLP seems slightly better than that from CSP. This is assumed due to the consideration of the MCS physics in MLP estimation because CSP does not consider the internal interactions, except for the entry and exit positions and directions. This leads to the hypothesis that tracing the proton path in a non-uniform media such as the human body would further improve the pCT reconstruction of Figure 5.

In addition to the possible improvement by tracing the proton path through the patient-specific tissue structure, another possible improvement may be obtained by statistical model-based image reconstruction. For example, for the PWLS reconstruction algorithm, the data variance contains the ground truth of the energy loss straggling via equation (9) when the energy loss is less than 20%. This can be further refined for cases of energy losses larger than 20% of the initial energy. For these cases, the theory of Tschalar (1968) would provide a more accurate description of the process than the Gaussian distribution. The variance of the energy loss distribution in Tschalar's theory can be expressed by the differential equation as:

$$\frac{d}{dx}\sigma_T^2(x) = \kappa_2(x) - 2\left(\frac{d}{dE}\kappa_1(E(x))\right)\sigma_T^2(x) + \text{higher order terms} \tag{21}$$

where

$$\kappa_2(x) = \eta_e K \frac{1 - 1/2 \cdot \beta^2\left(E(E_{in}, x)\right)}{1 - \beta^2\left(E(E_{in}, x)\right)} \tag{22}$$

and $\kappa_1(E(x))$ is identical to the stopping power given by the Bethe Bloch formula (5), and the higher-order terms contain higher-order derivations of $\kappa_1(E(x))$ with respect to energy.

In conclusion, pCT has its great clinical potential to improve the utility of current proton beam therapy practice. Despite several challenges exist ahead in advancing pCT toward clinical use as described above, such as hardware construction and fast image reconstruction development, we have performed several studies to demonstrate the pCT potential. One is the pCT design study (Schulte et al. 2004), which describes the needed hardware components to achieve the desired performance of pCT for proton therapy. The second one is the analysis of image contrast (or density resolution), spatial resolution and dosage for the pCT design of Figure 1 (Satogata et al. 2003; Schulte et al. 2005). The third one is the pCT instrumentation progress (Sadrozinski et al. 2003). The last one is our development of sophisticated image reconstruction algorithms which consider the data statistics and object-specific proton paths (Li et al. 2003, 2004, 2006). By these studies, we can conclude that a density resolution of 1-2% and a range uncertainty of the same order of magnitude (i.e., of 1 mm order) seem possible with proton doses of 10 mGy or less, which is comparable to doses stated for cone beam xCT with keV X-ray beams and an order of magnitude less than the dose required to resolve soft tissues with megavoltage X-ray photon radiation.

ACKNOWLEDGEMENT

This work was supported in part by the NIH National Cancer Institute under Grant No. CA082402. The authors would like to thank all colleagues (S. Peggs, K. Mueller, A. Wroe) of the pCT collaboration for their encouragement and invaluable advice.

REFERENCES

Agostinelli, S., Allison, J., Amako, K., Apostolakis, J., Araujo, H., Arce, P., Asai, M., Axen, D., Banerjee, S., and Barrand, G. 2003. GEANT4 – a simulation toolkit. Nucl. Instrum. Meth. Phys. Res. A 506: 250-303.

Bichsel, H., Groom, D.E., and Klein, S.R. 1972. *Passage of Charged Particles through Matter*. New York: McGraw-Hill, 42: 188-189, (Coordinating Editor: D.E. Gray; American Institute of Physics Handbook).

Bohr, N. 1948. The penetration of atomic particles through matter. K. Dan. Vidensk. Selsk, Mat. Fys. Med. 18: 1.

Cormack, A.M., and Koehler, A.M. 1976. Quantitative proton tomography: preliminary experiments. Phys. Med. Biol. 21: 560-569.

Dempster, A., Laird, N., and Rubin, D. 1977. Maximum likelihood from incomplete data via the EM algorithm. J. R. Stat. Soc. 39B: 1-38.

Groh, B.A., Siewerdsen, J.H., Drake, D.G., Wong, J.W., and Jaffray, D.A. 2002. A performance comparison of flat-panel imager-based MV and kV cone-beam CT. Med. Phys. 29: 967-975.

Hanson, K.M., Bradbury, J.N., Cannon, T.M., Hutson, R.L., Laubacher, D.B., Macek, R.J., Paciotti, M.A., and Taylor, C.A. 1981. Computed tomography using proton energy loss. Phys. Med. Biol. 26: 965-983.

Hanson, K.M., Bradbury, J.N., Koeppe, R.A., Macek, R.J., Machen, D.R., Morgado, R., Paciotti, M.A., Sandford, S.A., and Steward, V.W. 1982. Proton computed tomography of human specimens. Phys. Med. Biol. 27: 25-36.

ICRU Report No. 44. 1989. *Tissue Substitutes in Radiation Dosimetry and Measurements*. International Commission on Radiation Units and Measurements, Bethesda, MD.

ICRU Report No. 49. 1993. *Stopping Powers and Ranges for Protons and Alpha Particles*. International Commission on Radiation Units and Measurements, Bethesda, MD.

Jaffray, D.A., Siewerdsen, J.H., Wong, J.W., and Martinez, A.A. 2002. Flat-panel cone-beam computed tomography for image-guided radiation therapy. Int. J. Radiat. Oncol. Biol. Phys. 53: 1337-1349.

Janni, J.F. 1982. Proton range-energy tables. Atomic Data and Nuclear Data Tables 27: 212-245.

Koehler, A.M. 1968. Proton radiography. Science 160: 303-304.

Koehler, A.M., and Steward, V.W. 1974. Proton radiographic detection of strokes. Nature 245: 38-40.

Leo, W.R. 1994. *Techniques for Nuclear and Particle Physics Experiments*. Springer Verlag, Berlin (pp.21).

Li, T., Liang, Z., Mueller, K., Heimann, J., Johnson, L.R., Sadrozinski, H.F.-W., Seiden, A., Williams, D.C., Zhang, L., Peggs, S., Satogata, T.J., Bashkirov, V., and Schulte, R.W. 2003. Reconstruction for proton computed tomography: a Monte Carlo study. Conference Record of IEEE Nuclear Science Symposium and Medical Imaging Conference 5, in CD-ROM (IEEE Publication).

Li, T. and Liang, Z. 2004. Reconstruction with most likely trajectory for proton computed tomography. SPIE Medical Imaging: Image Processing 5370: 2067-2074.

Li, T., Liang, Z., Singanallur, J., Satogata, T.J., Williams, D.C., and Schulte R.W. 2006. Reconstruction for proton computed tomography by tracing proton trajectories – a Monte Carlo study. Med. Phys. 33: 699-706.

Liang, Z., Jaszczak, R.J., and Greer, K.L. 1989. "On Bayesian image reconstruction from projections: uniform and non-uniform *a priori* source information. IEEE Trans. Med. Imag. 8: 227-235.

Liang, Z., Jaszczak, R.J., and Coleman E.R. 1991. On reconstruction and segmentation of piecewise continuous images. Inform. Proc. Med. Imag. 12: 94-104.

Liang, Z. and Ye, J. 1994. Reconstruction of object-specific attenuation map for quantitative SPECT. Conference Record of IEEE Nuclear Science Symposium and Medical Imaging Conference 2: 1231-1235 (IEEE Publication).

Luenberger, D.G. 1984. *Linear and Nonlinear Programming*. Addison-Wesley Publishing Company, MA.

Sadrozinski, H.F.-W., Bashkirov, V., Bruzzi, M., Johnson, L.R., Keeney, B., Ross, G., Schulte, R.W., Seiden, A., Shahnazi, K., Williams, D.C., and Zhang, L. 2003. Issues in proton computed tomography. Nucl. Instrum. Methods Phys. Res. A, 511: 275-281.

Satogata, T.J., Sadrozinski, H.F-W., Dilmanian, A., Peggs, S., and Ruggiero, A. 2003. Dose/Sensitivity in Proton Computed Tomography. Conference Record of IEEE Nuclear Science Symposium and Medical Imaging Conference 5, in CD-ROM (IEEE Publication).

Sauer, K., and Bouman, C. 1993. A local update strategy for iterative reconstruction form projections. IEEE Trans. Sig. Proc. 41: 534-548.

Schaffner, B., and Pedroni, E. 1998. The precision of proton range calculations in proton radiotherapy treatment planning: experimental verification of the relation between CT-HU and proton stopping power. Phys. Med. Biol. 43: 1579-1592.

Schneider, U., and Pedroni, E. 1994. Multiple Coulomb scattering and spatial resolution in proton radiography. Med. Phys. 21: 1657-1663.

Schneider, U., Besserer, J., Pemler, P., Dellert, M., Moosburger, M., Pedroni, E., and Kaser-Hotz, B. 2004. First proton radiography of an animal patient. Med. Phys. 31: 1046-1051.

Schulte, R.W., Bashkirov, V., Li, T., Liang, Z., Mueller, K., Heimann, J., Johnson, L.R., Keeney, B., Sadrozinski, H.F.-W., Seiden, A., Williams, D.C., Zhang, L., Li, Z., Peggs, S., Satogata, T.J., and Woody, C. 2004. Conceptual design of a proton computed tomography system for applications in proton radiation therapy. IEEE Trans. Nucl. Sci. 51: 866-872.

Schulte, R.W., Bashkirov, V., Klock, M., Li, T., Wroe, A., Evseev, I., Williams, D.C., and Satogata, T.J. 2005. Density resolution of proton computed tomography. Med. Phys. 32: 1035-1046.

Seppi, E.J., Munro, P., Johnsen, S.W., Shapiro, E.G., Tognina, C., Jones, D., Pavkovich, J.M., Webb, C., Mollov, I., Partain, L.D., and Colbeth, R.E. 2003. Megavoltage cone-beam computed tomography using a high-efficiency image receptor. Int. J. Radiat. Oncol. Biol. Phys. 55: 793-803.

Tschalar, C. 1968. Straggling distributions of large energy losses. Nucl. Instrum. Methods 61: 141-156.

Tschalar, C. 1968. Straggling distributions of extremely large energy losses. Nucl. Instrum. Methods 64: 237-243.

Williams, D.C. 2004. The most likely path of an energetic charged particle through a uniform medium. Phys. Med. Biol. 49: 2899-2911.

FIGURE CAPTIONS:

Figure 1: Schematic illustration of an idealized single-proton-tracking pCT scanner. Protons with known incident energy E_{in} are individually recorded by the four planes of position-sensitive silicon detectors which forms the scanner reference system (t, u, v). These four planar detectors provide positions as well as azimuth and declination angles of the protons in front and behind the object. The exit energy E_{out} of each proton is recorded with a segmented calorimeter in coincidence with its position and angle information in planes 3 and 4. For a complete scan, the object is traversed by broad proton beams from many different projection angles ϕ. For parallel beam incidence, ϕ may go from 0 to 180 degrees. For cone-beam incidence (i.e., protons come from a point source), ϕ may go a full circle around the object. The resulting parallel- or cone-beam data set allows reconstruction of the relative electron density distribution inside the object reference system (x, y, z).

Figure 2: Spatial distribution of the average energy of protons hitting all four SSD planes (left). The image of the object can be clearly seen. Areas A and B are selected to compare with the results from the GEANT4 MC simulation. On the right shows the comparison between experimental angular distributions (points) and GEANT4 MC simulated histograms) in area A (through the object) and B (the wax degrader only).

Figure 3: Schematic illustration of proton path for the pCT scanner of Figure 1. The path of protons traveling inside an object is determined by a multitude of individual scattering events leading to a zigzag path (red). Both the position and direction of entry and exit proton are registered. Given the object boundary, the intersecting points A and B of a proton with the object can be obtained. While the intersecting points are sufficient to estimate the straight line

path (black) of the proton, additional knowledge of the entry and exit directions permits estimation of the most likely path (blue line) (Williams, 2004).

Figure 4: Most likely trajectories calculated with different settings of displacement t_1 and deflection angle θ_1 of Figure 3. The proton entries at t=0. Two exist positions are assumed, where eleven exist directions are measured for one exist position and five directions are measured at another exist position.

Figure 5: Top middle picture is the elliptical phantom consisting of an outer shell of bone density (1), an elliptical interior of water density (2), and two sets of strip patterns with either bone density (white) or air density (black). The strip densities of the patterns (listed by number) are: 2 lp cm^{-1} (3, 11), 2.5 lp cm^{-1} (4, 12), 3 lp cm^{-1} (5, 13), 3.5 lp cm^{-1} (6, 14), 4 lp cm^{-1} (7, 15), 4.5 lp cm^{-1} (8, 16), 5 lp cm^{-1} (9, 17), and 6 lp cm^{-1} (10, 18). Top right picture shows the FBP result after the SLPs were interpolated onto regular grids in sinogram space. Top right picture shows the ART result using the SLPs. Middle row pictures are the ART results by tracing the CSPs (left) and MLPs (right), respectively. Bottom pictures are the zoomed results of the strips of #15 in the ART results of the middle row. A square box indicates the strips of #15 in the phantom.

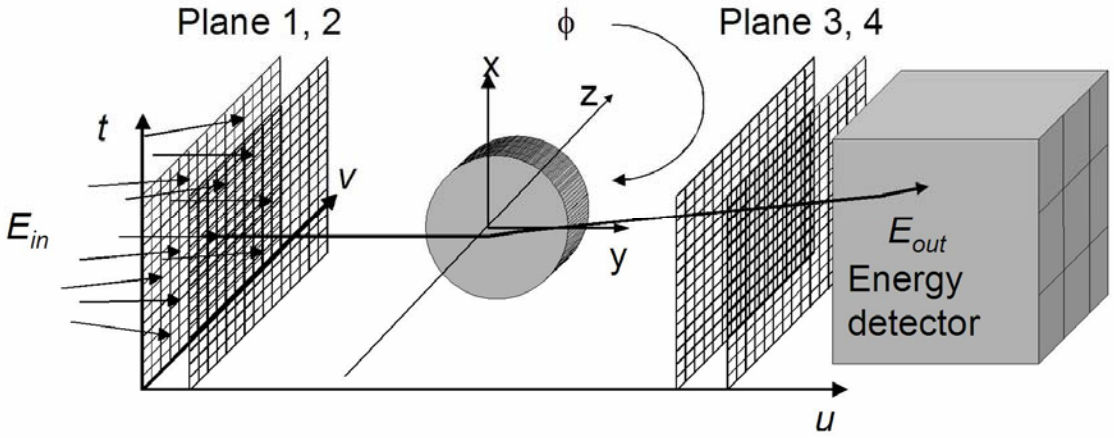

Figure 1: Schematic illustration of an idealized single-proton-tracking pCT scanner. Protons with known incident energy E_{in} are individually recorded by the four planes of position-sensitive silicon detectors which forms the scanner reference system (t, u, v). These four planar detectors provide positions as well as azimuth and declination angles of the protons in front and behind the object. The exit energy E_{out} of each proton is recorded with a segmented calorimeter in coincidence with its position and angle information in planes 3 and 4. For a complete scan, the object is traversed by broad proton beams from many different projection angles ϕ. For parallel beam incidence, ϕ may go from 0 to 180 degrees. For cone-beam incidence (i.e., protons come from a point source), ϕ may go a full circle around the object. The resulting parallel- or cone-beam data set allows reconstruction of the relative electron density distribution inside the object reference system (x, y, z).

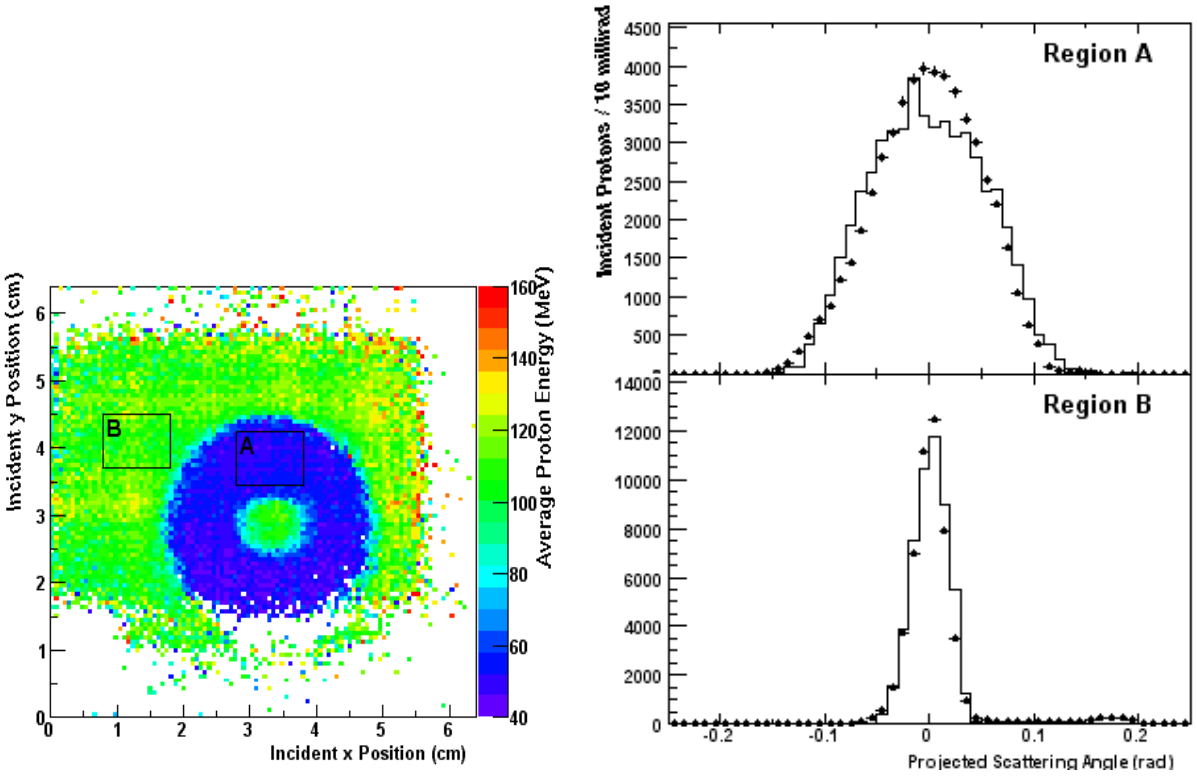

Figure 2: Spatial distribution of the average energy of protons hitting all four SSD planes (left). The image of the object can be clearly seen. Areas A and B are selected to compare with the results from the GEANT4 MC simulation. On the right shows the comparison between experimental angular distributions (points) and GEANT4 MC simulated histograms) in area A (through the object) and B (the wax degrader only).

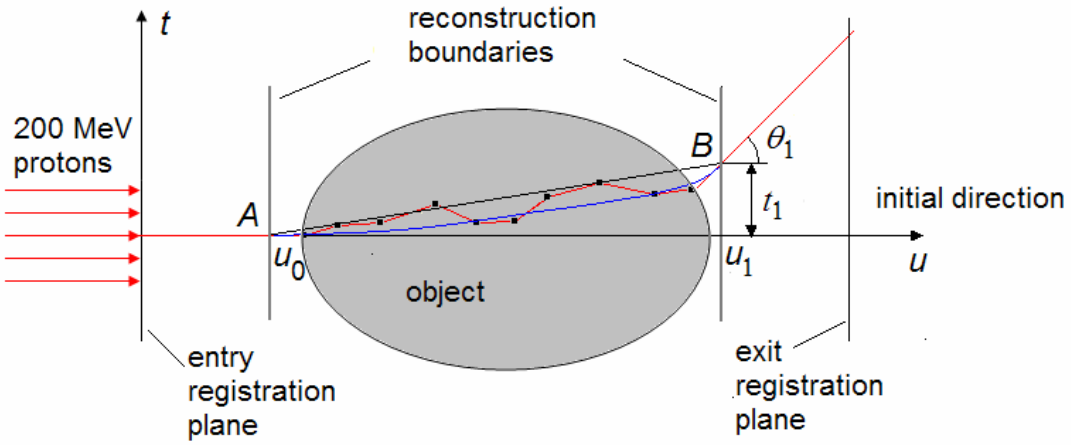

Figure 3: Schematic illustration of proton path for the pCT scanner of Figure 1. The path of protons traveling inside an object is determined by a multitude of individual scattering events leading to a zigzag path (red). Both the position and direction of entry and exit proton are registered. Given the object boundary, the intersecting points *A* and *B* of a proton with the object can be obtained. While the intersecting points are sufficient to estimate the straight line path (black) of the proton, additional knowledge of the entry and exit directions permits estimation of the most likely path (blue line) (Williams, 2004).

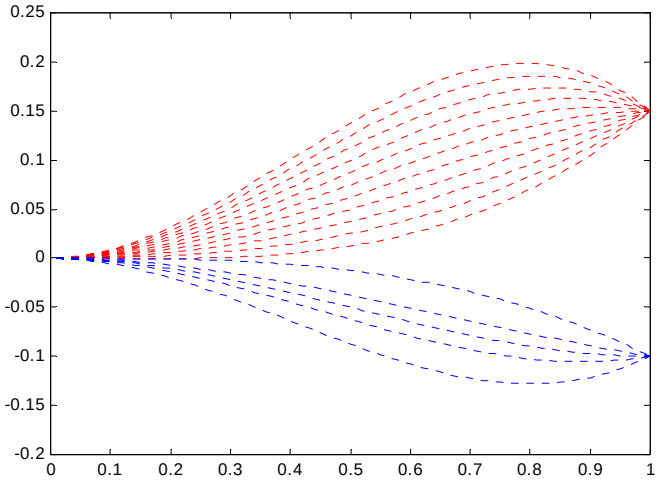

Figure 4: Most likely trajectories calculated with different settings of displacement t_1 and deflection angle θ_1 of Figure 3. The proton entries at t=0. Two exist positions are assumed, where eleven exist directions are measured for one exist position and five directions are measured at another exist position.

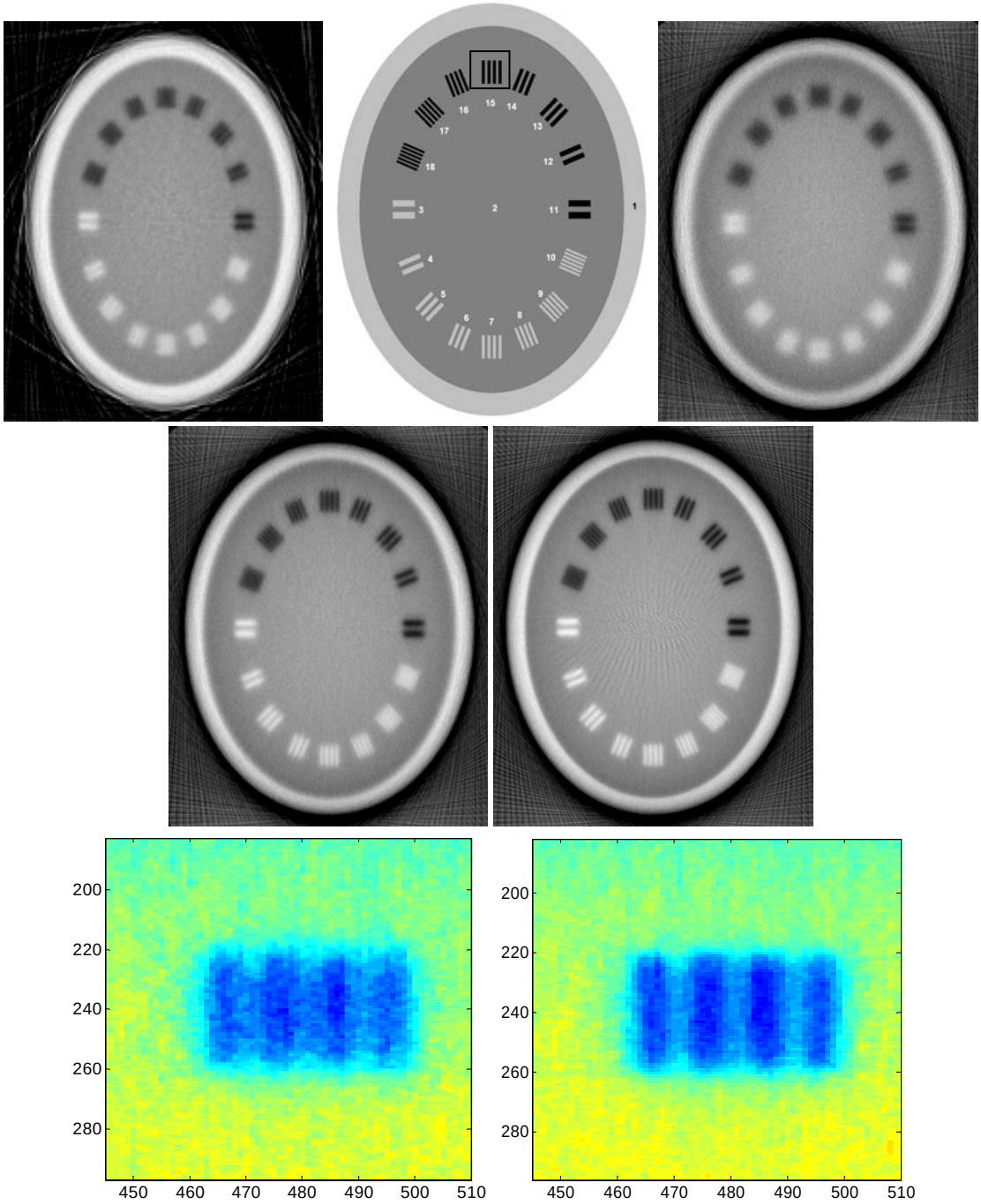

Figure 5: Top middle picture is the elliptical phantom consisting of an outer shell of bone density (1), an elliptical interior of water density (2), and two sets of strip patterns with either bone density (white) or air density (black). The strip densities of the patterns (listed by number) are: 2 lp cm^{-1} (3, 11), 2.5 lp cm^{-1} (4, 12), 3 lp cm^{-1} (5, 13), 3.5 lp cm^{-1} (6, 14), 4 lp cm^{-1} (7, 15), 4.5 lp cm^{-1} (8, 16), 5 lp cm^{-1} (9, 17), and 6 lp cm^{-1} (10, 18). Top right picture shows the FBP result after the SLPs were interpolated onto regular grids in sinogram space. Top right picture shows the ART result using the SLPs. Middle row pictures are the ART results by tracing the CSPs (left) and MLPs (right), respectively. Bottom pictures are the zoomed results of the strips of #15 in the ART results of the middle row. A square box indicates the strips of #15 in the phantom.